

High-precision control of a robotic arm using frequency-based data-driven methods[☆]

Philippe Schuchert, Alireza Karimi^{*}

Laboratoire d'Automatique, École Polytechnique Fédérale de Lausanne (EPFL), Switzerland

ARTICLE INFO

Keywords:

Data-driven control
Frequency-based control
Mechatronics
Linear-parameter-varying control
High-precision robots

ABSTRACT

Next-generation motion control systems require fast and precise control. However, advanced control strategies often rely on complex and costly system models. Data-driven methods have been proposed to design high-performance controllers without requiring a parametric model of the system. In particular, methods using frequency response functions (FRFs) have been widely applied to mechatronic systems due to their good performance, and the industry's familiarity with obtaining FRFs. This paper applies a recently developed method to design a controller for an industrial robotic arm with three translational degrees of freedom, using only the FRF of the robot around different operating points. Focused on motion control, the objective is to attain the desired reference tracking performance through the design of a linear-parameter-varying (LPV) two-degree-of-freedom (2DoF) controller. Performance is further improved by tuning an additional filter to compensate for inaccuracies in the transmission.

1. Introduction

Robotic arms are machines used for various applications in the manufacturing industry, such as welding, painting and coating, assembly, metrology, and quality inspection. Fast and precise movements are a requirement for next-generation motion control systems to increase the throughput of the manufacturing process. To this day, simple control architectures such as PID control in joint space are often the default approach but they may not be sufficient to achieve the desired performance (Chen, 1987), and improved synthesis methods are required to meet ever-increasing performance demands (Oomen, 2018).

To tackle this challenge, a wealth of modern control strategies has been proposed. For example, the inverse dynamics can be computed and used to cancel undesired dynamics, with additional filters to compensate for small mismatches (De Luca, Siciliano, & Zollo, 2005). Implementing a control law with gravity compensation requires access to low-level measurements and inputs, such as the torque applied by the motor. This may not always be possible and is especially challenging when integrating off-the-shelf components. For example, a motor may come with a proprietary driver that cannot be fully modified (Ahanda, Aba, Melingui, Zobo, & Merzouki, 2022), e.g. only the PID coefficients that can be changed. A simple and alternative motion control pipeline

in such a case is to compute desired reference joint positions using the inverse kinematics of the robotic arm and forward these references to the motor driver.

For robotic arms, a direct drive approach for joint control is seldom used, as large and expensive motors would be required to produce the torque required to move the system. Instead, reductions are often employed to act as a torque multiplier. However, this induces additional resonant modes due to the stiffness of the reduction, and other possible sources of mismatch. This discrepancy is problematic in high-precision applications, requiring additional mechanisms to regulate the joints to the desired joint references.

To address the challenges posed by joint control discrepancies in high-precision applications, additional strategies must be employed to improve performance of motion control systems, especially when high-precision motion control is sought. A common approach is to have different performance specifications for regulation or reference tracking, which is commonly achieved using a two-degree-of-freedom controller. For example, the feedforward path can exploit techniques such as input shaping (Singer & Seering, 1990; Vaughan, Yano, & Singhose, 2008), or model inversion (Boerlage, Steinbuch, Lambrechts, & van de Wal, 2003). This can offer significant benefits, as the reference is often smooth and consists mainly of slow varying trajectories,

[☆] This work is funded by INNOSUISSE, Switzerland under grant no. 48289.1 IP-ENG and the National Centre of Competence in Research, Switzerland under grant no. 51NF40 180545 NCCR Automation.

^{*} Corresponding author.

E-mail address: alireza.karimi@epfl.ch (A. Karimi).

<https://doi.org/10.1016/j.conengprac.2024.106175>

Received 12 April 2024; Received in revised form 12 November 2024; Accepted 13 November 2024

Available online 28 November 2024

0967-0661/© 2024 The Authors. Published by Elsevier Ltd. This is an open access article under the CC BY license (<http://creativecommons.org/licenses/by/4.0/>).

whereas noise and various unmodelled dynamics may have a significantly different spectrum than the reference. Exploiting this knowledge can significantly improve performance. Furthermore, the dynamics of machines may change depending on the operating conditions, therefore requiring nonlinear models and control design tools.

Techniques such as gain-scheduling (Rugh & Shamma, 2000) and LPV techniques (Hoffmann & Werner, 2015) have been proposed, and are widely used, to design high-performance nonlinear controllers while keeping the formalism of linear time-invariant systems. Designing a controller using these techniques relies on an accurate model of the system's dynamics. First principle models may fail to capture the intricacies of the dynamics of a real system, and obtaining a control-relevant model through a system identification step can be more costly than designing the controller itself (Gevers, 2005). This cost becomes even more significant if the objective is to obtain an accurate LPV model, and therefore obtaining a suitable model is often the most challenging part when designing an LPV controller. On the other hand, FRFs have been proven to be an effective data-driven way of representing mechanical systems, including systems with many resonant modes (Pintelon & Schoukens, 2012). FRFs are simple and easy to obtain, well understood in the industry, and have been extensively used to tune controllers using classical control theory tools such as loop shaping using Bode plots or Nichols charts. Using efficient numerical optimizers, recent methods have been proposed to synthesize controllers directly from the FRF, e.g., Schuchert, Gupta, and Karimi (2024). Modern frequency-domain methods have been shown to achieve good performance (Bagherieh, Shah, & Horowitz, 2018; Kammer & Karimi, 2017), with proposed extensions to LPV controller synthesis (Bloemers, Tóth, & Oomen, 2019; Schuchert & Karimi, 2023), further affirming their efficacy.

This paper proposes a novel LPV control strategy for robotic arms used for high-precision motion control applications in the manufacturing industry, based on the approach described in Schuchert et al. (2024) which focuses on a Cartesian robot and designs a series of SISO controllers. A significant advantage of the proposed approach compared to other modern controller synthesis methods is that it eliminates the need for an expensive parametric LPV model of the system. Instead, only local frequency responses around different operating points are used. This removes the costly parametric identification step and greatly simplifies the modelling phase without compromising the resulting performance, as demonstrated in a real application. Moreover, the final controller can be obtained by solving a series of convex problems, and off-the-shelf numerical optimizers can be used, which significantly speeds up the implementation of the proposed approach over other similar LPV control synthesis methods. Unlike (Schuchert et al., 2024), this paper uses cylindrical coordinates computed from the joint positions to describe the tool position. The desired tracking performance is achieved by tuning a MIMO LPV 2DoF controller, which also considers the coupling in the robot's dynamics. On top of this, another filter is used to compensate for transmission inaccuracies.

This paper is organized as follows: Section 2 describes the robotic arm and outlines the proposed solution. A compensation scheme for strain-wave gears is discussed in Section 3, and Section 4 deals with the spectral analysis of the system. Section 5 details the controller synthesis and finally, Section 6 demonstrates the application to the real robotic arm.

Notations: The zero vector and identity matrix of appropriate size are denoted $\mathbf{0}$ and I , respectively. The inverse transpose of a matrix M is denoted M^{-T} . The conjugate transpose of the diagonally opposed element in a square matrix is denoted using a \star . The vector created by vertically stacking a and b is denoted using $[a; b]$. The set of stable and bounded on the unit circle transfer functions is denoted \mathcal{RH}_∞ . The two or infinity norms of an LTI system are denoted $\|\cdot\|_2$ and $\|\cdot\|_\infty$, respectively.

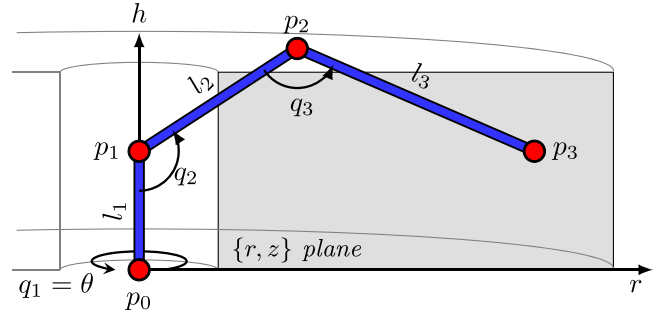


Fig. 1. Schematic representation of the robotic arm.

2. System description

A robotic arm is used to position the end-effector with high accuracy. The operating volume of this robot is a cylindrical shell with an inner radius of 150 mm, outer radius of 550 mm, and height of 250 mm. The working volume is denoted using \mathbb{P} , and the position of the end-effector is denoted p . Three joints are used to move the end-effector in this operating volume: the first joint is used to rotate the arm around the cylinder's axis of rotation, and the other two joints are used to move in the plane formed by the radius and height of the cylinder. This robot has three translational degree of freedom, each corresponding to one direction in which the tool can move independently of the others. In this case, it is possible to associate a Cartesian coordinate system to each degree of freedom of the tool. A schematic illustration of the robotic arm is presented in Fig. 1. Unfortunately, due to confidentiality agreements with the implementation partner, a picture of the real system cannot be provided.

Each joint is actuated using a motor and corresponding motor driver given by the manufacturer, along with a strain-wave gear, to increase torque and precision.

Assumption 1. The motor controller is either inaccessible, not fully exposed, or unknown.

Assumption 1 can happen when low-level access to the motor drivers is not possible. This is prone to happen when using off-the-shelf components and a motor-controller structure is imposed (e.g., PID with additional notch filters) by the manufacturer or for reasons as discussed in Ahanda et al. (2022). In the present case, the motor driver is only partially exposed: coefficients from the motor controller can be changed, but a different architecture cannot be implemented.

The joint positions are measured using additional encoders $q = [q_1; q_2; q_3]$. Control of this robot's end-effector position will not be done in tool space; instead, cylindrical coordinates are used:

$$y = [r; \theta; h] \quad (1)$$

where $\theta = q_1$, to exploit the rotational symmetry of the robot. The tool position (using cylindrical coordinates) corresponds to the operating point $p = y$, and the control objective is to precisely track a given reference y_d .

The forward kinematics (F.K.), mapping the joint angles to a position in the $\{r, h\}$ plane, are given by

$$p_1 = [0; l_1] \quad (2a)$$

$$p_2 = p_1 + l_2 \cdot [\sin(q_2); -\cos(q_2)] \quad (2b)$$

$$p_3 = p_2 + l_3 \cdot [-\sin(q_2 + q_3); \cos(q_2 + q_3)] \\ = [r; h] \quad (2c)$$

For this system, it is required that the third joint angle satisfies $0 \leq q_3 \leq \pi$. The inverse kinematics (I.K.), mapping a point in the

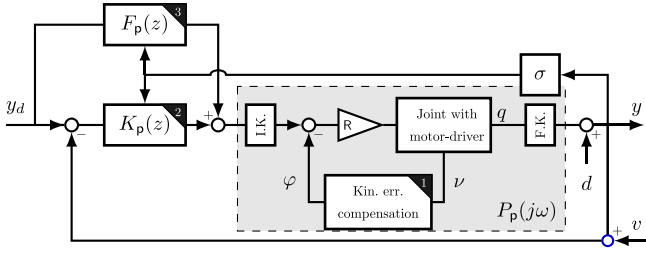


Fig. 2. Block diagram of the control loop architecture. The order in which the different elements should be tuned is indicated in the top right corner. The gain R corresponds to the reduction ratio of the strain-wave gears.

cylindrical coordinates to joint angles, are then uniquely determined and given by

$$q_3 = \cos^{-1} \left(\frac{l_3^2 + l_2^2 - \|p_{31}\|^2}{2l_2l_3} \right) \quad (3a)$$

$$q_2 = \cos^{-1} \left(\frac{l_2^2 + \|p_{31}\|^2 - l_3^2}{2l_2\|p_{31}\|} \right) + \angle\{p_{31}\} + \frac{\pi}{2} \quad (3b)$$

where $p_{31} = p_3 - p_1$, and $\angle\{p_{31}\}$ corresponds to the angle formed between the vectors p_3 and p_1 , and is defined as $\angle\{p_{31}\} = \text{atan2}(b, a)$ where a, b are, respectively, the first and second element of the vector p_{31} . The function atan2 is used to denote the 2-argument arctangent.

For motion control, a common strategy is to use the inverse kinematics to compute the appropriate reference angles for the joints. These reference angles are then transmitted to a lower-level motor position control loop, which drives the joints to the desired positions. In this paper, an additional loop with a 2DoF controller is introduced to improve performance and address the dynamics of the reductions and coupling between joints. Note that 2DoF refers to the structure of the controller and is not related to the degrees of freedom of the robot.

Although the motor-loop may be well-tuned with a larger-than-required control bandwidth, this does not necessarily translate into adequate performance in tool-space, as will be clarified later on and illustrated in Fig. 5. A 2DoF controller architecture is selected to attain the desired tracking performance. This control structure consists of two separate transfer functions: a controller for closed-loop feedback, and a feedforward filter to improve tracking performance.

To obtain improved performance, an LPV control law, function of a scheduling parameter $\sigma(p)$, is used for each of the transfer functions. The scheduling parameter will be a function of the operating point, and therefore the controller is often referred to as a quasi-LPV controller as $p (= y)$, corresponding to the tool position, is a state of the system's dynamics. The block diagram of the proposed approach is depicted in Fig. 2 and includes an additional filter to compensate for inaccuracies in the transmission, as described in the next section.

This controller takes as input the reference and measured positions $\{y_d, y\}$ and computes a signal u sent to the inverse kinematics, which is mapped to the reference joint positions for the motor loop. The additional filter in the inner-loop computes an offset of the motor reference to compensate for inaccuracies of the transmission and is detailed in the next section.

3. Kinematic error compensation

Before tuning the LPV 2DoF controller, this robot requires additional attention in joint space. A strain-wave gear reduction is used to increase the torque and the accuracy of the motor. Reductions are often treated as a simple gain, i.e.,

$$R_i q_i \approx v_i \quad i \in \{1, 2, 3\} \quad (4)$$

where v_i, R_i are the motor position and reduction ratio of the i th joint, respectively. This idealized model does not hold in practice, especially

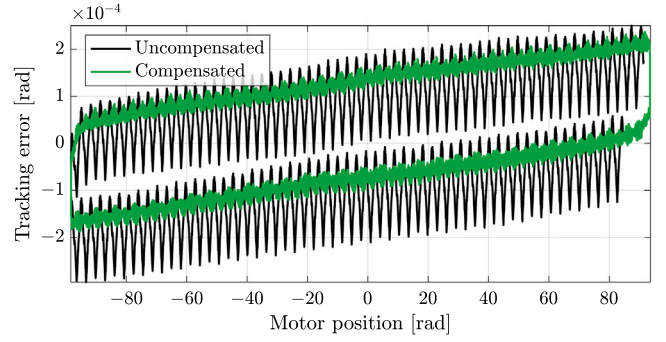


Fig. 3. Open-loop tracking performance of θ at low speeds with and without kinematic compensation of the strain-wave gear.

when high precision is required, as reductions introduce additional dynamics to the system. In particular, it has been noted in Ghorbel, Gandhi, and Alpeter (2001) that errors from strain-wave gears can be classified into two major sources: a static part when $|\dot{v}_i| \approx 0$, and a flexibility-induced component depending on the dynamics. The nonlinear static part is denoted as the pure component:

$$\varepsilon_i(v_i) = R_i q_i - v_i \quad i \in \{1, 2, 3\} \quad (5)$$

and is especially visible when moving at low to moderate speeds. For example, when rotating the first joint, high-frequency oscillations can be observed with a peak-to-peak magnitude of $\approx 2 \cdot 10^{-4}$ rad can be observed, along with other low-frequency trends. As noted by Ghorbel et al. (2001), this perturbation is only a function of the actual motor position and therefore can be modelled and compensated. To compensate for this nonlinear source of errors, the approach proposed in Yamamoto et al. (2009) is used: derive a parametric representation $\hat{\varepsilon}$ and compensate the pure kinematic errors by systematically offsetting the motor reference positions as shown in Fig. 2 using $\varphi = [\varphi_1; \varphi_2; \varphi_3]$ where

$$\varphi_i(v_i) = R_i \cdot \hat{\varepsilon}_i(v_i) \quad i \in \{1, 2, 3\} \quad (6)$$

To compute $\hat{\varepsilon}$, a data set is collected by moving each joint very slowly from one side of the possible joint range to the other. The joints are moved slowly to avoid exciting the flexibility-induced dynamics, and the data is filtered to include only high-frequency trends, as the control loops will reject low-frequency trends. The pure kinematic errors are modelled using a Fourier series, as proposed in Yamamoto et al. (2009):

$$\hat{\varepsilon}_i(v_i) = \sum_{k=1}^N A_k \sin(2kv) + B_k \cos(2kv) \quad (7)$$

The coefficients A_k, B_k are then obtained by least-squares fit, minimizing $\|\varepsilon_i - \hat{\varepsilon}_i\|_2$. The proposed compensation for the pure kinematic error is then implemented for each joint on the robot. To assess performance, the joints are moved back and forth. For conciseness, only data from the first joint is shown, as the joint's performance directly translates into tracking performance of θ , as illustrated in Fig. 3.

As can be seen, the tracking error (in joint space) is significantly reduced with this relatively simple scheme. It is worth noting that the flexibility-induced component are compensated using the outer loop with the 2DoF controllers.

4. Frequency function estimation

The system's dynamics over the whole operating range are not linear but, while working around a local operating point p , can be locally well approximated using a linear system. This leads to the following assumption:

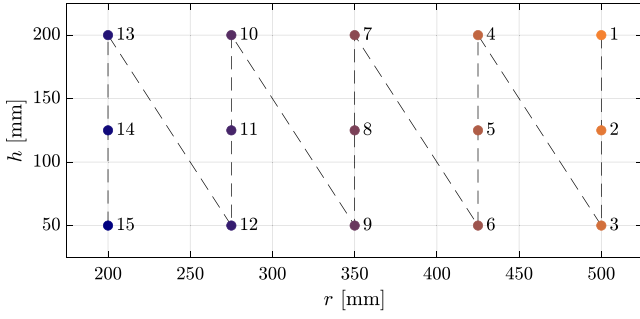


Fig. 4. Points in the $\{r, h\}$ plane where the FRF is obtained.

Assumption 2. The frozen dynamics representation at each operating point remains a valid description of the system.

Remark 1. Assumption 2 may seem very restrictive, as the dynamics are a function of the operating points and therefore intended to change. For the robot system considered, the dynamics vary significantly only over large distances in the operating space. Physical limitations will put a limit at which the operating space can be traversed, in turn limiting the rate of change of the dynamics. For the system considered, experimental results justify this assumption as well.

Around each operating point, the FRF can be obtained from input-output data. A total of 15 different local data sets are collected for each axis at positions described in Fig. 4 around operating points $p \in \mathbb{P}$. In general, a dense regular grid of the operating space is a good starting choice. These operating points should be chosen such that any change in the dynamics is well reflected in the local FRFs. For example, if a resonant mode shifts from one frequency to another between different points in the operating space, sufficient intermediate models must be taken to highlight this change. In the present case, the operating points are chosen on a regular grid in the $\{r, z\}$ plane. Due to the rotational symmetry of the robot, it is sufficient to obtain the dynamics around a fixed θ , and here $\theta = 0$ is chosen.

The FRF is obtained at small velocities, since the robot is designed to track references at relatively low speeds. Any effects arising due to rapid movements, such as Coriolis forces, will be modelled as uncertainty in the control design.

Each data set consists of 60 s of input and output measurements, using a sampling time of $T_s = 10^{-3}$ s, which also corresponds to the sampling time of the control loops, and represents a total of $N = 6 \cdot 10^4$ data points. The input u for the open-loop identification is a *multisine* signal with random phase given by:

$$u(t) = u_0 + \sum_{k=1}^{N/2} \left(\frac{\beta}{k} \right)^\gamma \sin(2\pi k(t - a_k)/N) \quad (8)$$

where a_k is a random integer in $\{1, \dots, N-1\}$. This signal is rich, i.e. it excites all frequencies, and further properties of *multisine* signals can be found in Pintelon and Schoukens (2012). The constants γ and β are chosen such that all frequencies are well excited, but not too large to saturate the motor's voltage and current.

The objective of this paper is to design controllers using a direct data-driven approach, avoiding the potentially costly intermediate modelling phase. This will be achieved through a controller synthesis method that requires only the FRF to model the system dynamics, with more details provided in Section 5. Therefore, the local open-loop FRF $P_p(j\omega)$ must first be computed at every frequency ω . This is achieved in this case using spectral analysis (Pintelon & Schoukens, 2012)

$$P_p(e^{j\omega}) = \left[\sum_{k=0}^{N-1} \mathbb{Y}(k) e^{-j\omega T_s k} \right] \left[\sum_{k=0}^{N-1} \mathbb{U}(k) e^{-j\omega T_s k} \right]^{-1} \quad (9)$$

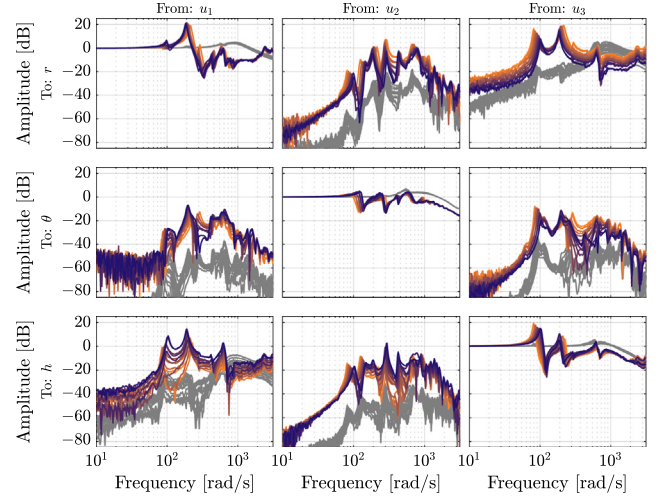


Fig. 5. Magnitude response of $P_p(j\omega)$ at different operating points p . Erroneous FRF computed from motor positions, in grey, highlights that even if the motor loop is well-tuned, significant problems can arise during joint control. (For interpretation of the references to colour in this figure, the reader is referred to the web version of this article.)

with additional averaging done to reduce the variance. Each column of $\mathbb{U}(k)$ and $\mathbb{Y}(k)$ represents respectively the inputs and the outputs at sample k from one experiment. One experiment consists of applying $u(t)$ to one of the directions while keeping the other two input constants. These two constants inputs and the value u_0 naturally correspond to the operating point p . A total of 3 different experiments are needed to extract $P_p(e^{j\omega})$ from data. Remark that a rich signal is required, for example as proposed in (8), as otherwise $\mathbb{U}(k)e^{-j\omega T_s k}$ may be singular for some frequencies. The frequency response of the models around various operating points is reported in Fig. 5. Note that the FRF is obtained with the filter φ already implemented.

To showcase that the motor loop is well-tuned, an (erroneous) FRF of the end-effector dynamics, computed based using R_v instead of q in the forward kinematics, is indicated using a grey colour in Fig. 5. The (erroneous) FRF computed from the motor positions is well-behaved, in the sense that the FRFs are well decoupled with the diagonal dynamics similar to a second-order system with large control bandwidth, and the off-diagonal terms are small compared to the diagonal terms but do not correspond to the true end-effector dynamics. The low-frequency behaviour of the motor loop correlates well with the behaviour of the joint, as expected, but high-frequency behaviour differs significantly.

This highlights that, even if the motor loop is well-tuned, significant problems can arise when closing a loop. Moreover, a performance comparison will be used to showcase that closing the loop using the 2DoF controller results in significantly better performance than the open-loop using only the motor controller.

From the magnitude response shown in Fig. 5, it can be seen that the DC-gain of the system is approximately the identity. This is expected, as given enough time, the motor loop will drive the system to the correct reference position in the tool space. Compliance of the robot can be seen with the multiple pronounced resonant modes, starting at frequency $\omega = 10^2$ rad/s. The FRFs are coloured at each operating point using the corresponding colour given in Fig. 4. It can be seen from the colour that the frequency of the peaks correlates with the r position at which the spectral identification was done. Finally, note that the dynamics of $\{r, h\}$ have relatively strong couplings, whereas the coupling of θ with the other inputs is less pronounced. These many resonances are traditionally not addressed as they are difficult to explain using first principle approaches and, coupled with strong couplings, can result in a significant performance loss.

5. Controller design

The synthesis problem is split into two parts. First, the feedback controller design problem is framed as a mixed-norm mixed-sensitivity problem. Once this controller is designed, the feedforward filter is synthesized to minimize the tracking error.

To keep the notation short, a discrete-time LTI system with state-space matrices A, B, C, D is denoted by

$$\left[\begin{array}{c|c} A & B \\ \hline C & D \end{array} \right] := C(zI - A)^{-1}B + D \quad (10)$$

5.1. Feedback controller design

The feedback controller design is formulated as a mixed-norm mixed-sensitivity control design, with the design objective to reject a step disturbance. In this case, the objective of the feedback loop is to minimize the average impact of the disturbance d (see block diagram in Fig. 2), with corresponding spectrum W_o , onto the output y . This is equivalent to minimizing

$$\min_K \overline{J_p} \quad (11a)$$

$$\|W_o T_{yd}\|_2^2 \leq J_p \quad \forall p \in \mathbb{P} \quad (11b)$$

where $\overline{J_p}$ is the average value of J_p around the different operating points $p \in \mathbb{P}$, and the transfer-function from d to y is given by

$$T_{yd} = (I + P_p K_p)^{-1} \quad (12)$$

The disturbance is chosen as a step-signal, therefore:

$$W_o = z/(z - 1)I \quad (13)$$

An integrator is required in the controller to reject the step disturbance at steady state. Assuming that the feedback controller can be factored as

$$K_p = X_p Y_p^{-1} \quad (14)$$

this can be obtained using

$$Y_p(z)|_{z=1} = \mathbf{0} \quad (15)$$

To ensure operational reliability, it is crucial to account for various sources of uncertainties, including Coriolis forces during rapid movements, changes over the machine's lifespan, the introduction of new tools, and component replacements by end-users. Such models should ideally be included in the set of identified models, but since they are not known in advance, this uncertainty is modelled as a lumped multiplicative uncertainty: $G(I + \Delta W_2)$, where $\|\Delta\|_\infty \leq 1$. Robustness to these uncertainties can be achieved using an \mathcal{H}_∞ constraints, see Skogestad and Postlethwaite (2005), and is enforced in the design using

$$\|W_2 T_{yv}\|_\infty \leq 1 \quad \forall p \in \mathbb{P} \quad (16)$$

where W_2 is the inverse of a low-pass filter and

$$T_{yv} = P_p K_p (I + P_p K_p)^{-1} \quad (17)$$

5.1.1. Control synthesis problem

Collecting the performance objective and robustness requirements, the aim is to find a feedback controller $K_p = X_p Y_p^{-1}$ minimizing the following mixed-norm synthesis problem:

$$\min_{K_p} \overline{J_p} \quad (18a)$$

subject to

$$Y_p(z)|_{z=1} = \mathbf{0} \quad (18b)$$

$$\|W_1 T_{yd}\|_2^2 \leq J_p \quad \forall p \in \mathbb{P} \quad (18c)$$

$$\|W_2 T_{yv}\|_\infty \leq 1 \quad \forall p \in \mathbb{P} \quad (18d)$$

Solving this optimization problem is, in general, challenging, especially when no parametric model is available. A recent approach (Schuchert et al., 2024) has proposed a solution to this problem using only the FRF of the system $P_p(j\omega)$. In essence, this method formulates the synthesis problem using the fact that the \mathcal{H}_2 and \mathcal{H}_∞ norms can be formulated in the frequency domain. If T corresponds to a stable discrete-time system, then for the \mathcal{H}_∞ norm

$$\|T\|_\infty^2 = \sup_{\omega \in \Omega} \overline{\sigma}(T^*(j\omega)T(j\omega)), \quad (19)$$

where $\overline{\sigma}(\cdot)$ is the largest singular value, and for the \mathcal{H}_2 norm

$$\|T\|_2^2 = \frac{1}{2\pi T_s} \int_{\Omega} \text{trace}(T^*(j\omega)T(j\omega)) d\omega. \quad (20)$$

Minimizing these two norms is a non-convex optimization problem. Instead, Schuchert et al. (2024) focuses on finding a Linear Matrix Inequality (LMI) such that $T^*(j\omega)T(j\omega) \leq \Gamma(j\omega)$ holds. Minimizing a function of Γ , subject to the derived LMI, can then be used as a proxy to minimizing either the \mathcal{H}_2 or \mathcal{H}_∞ norm of T .

This approach formulates the synthesis problem as a minimization of the closed-loop norm of an augmented Linear Time-Invariant system denoted by G :

$$z = G_{11}w + G_{12}u \quad (21a)$$

$$y = G_{21}w + G_{22}u \quad (21b)$$

where w represents the exogenous disturbances and z corresponds to the performance channels. The closed-loop transfer function T_{zw} using $u = Ky$ can be expressed by a linear fractional transform \mathcal{F}_l :

$$\begin{aligned} T_{zw} &= \mathcal{F}_l(G, K) \\ &= G_{11} + G_{12}K(I - G_{22}K)^{-1}G_{21} \end{aligned} \quad (22)$$

The frequency response of the augmented system is denoted by

$$G(j\omega) = \left[\begin{array}{c|c} G_{11}(j\omega) & G_{12}(j\omega) \\ \hline G_{21}(j\omega) & G_{22}(j\omega) \end{array} \right] =: \left[\begin{array}{c|c} G_{11} & G_{12} \\ \hline G_{21} & G_{22} \end{array} \right] (j\omega)$$

Additionally, the notation $[\cdot](j\omega)$ will be used hereafter to indicate the evaluation of the entries of a matrix at frequency ω . Remark that under Assumption 2, the dynamics of the system are, around each operating point p , LTI. To apply (Schuchert et al., 2024) to the present problem, it is first required to find the augmented systems corresponding to the closed-loop transfer functions given in (18).

The augmented systems can be found by matching the desired closed-loop transfer functions with the definition of the lower-fractional transform (22):

$$G_d = \left[\begin{array}{c|c} W_o & -W_o P_p \\ \hline I & -P_p \end{array} \right] \quad (23a)$$

$$G_v = \left[\begin{array}{c|c} \mathbf{0} & W_2 P_p \\ \hline I & -P_p \end{array} \right] \quad (23b)$$

where $\mathcal{F}_l(G_d, K_p) = T_{yd}$ and $\mathcal{F}_l(G_v, K_p) = T_{yv}$. It should be clear that $G_d(j\omega)$ and $G_v(j\omega)$ are functions of the FRF $P_p(j\omega)$, obtained in Section 4, and the performance filters $W_o(j\omega)$, $W_2(j\omega)$ defined by the user, and therefore can be evaluated at frequency ω . Given a controller $K_p = X_p Y_p^{-1}$ where $X_p \in \mathcal{RH}_\infty$ and $Y_p \in \mathcal{RH}_\infty$ and for a fixed p , it is shown in Schuchert et al. (2024) that an inner-approximation in the controller parameters of

$$\min J_p \quad (24a)$$

subject to:

$$\|T_{zw}\|_2^2 \leq J_p \quad (24b)$$

is given by

$$\min J_p \quad (25a)$$

subject to:

$$\left[\begin{array}{c|c} \Gamma_p & (G_{11}\Phi + G_{12}X_p) \\ \hline \star & \Phi^* \Phi_c + \Phi_c^* \Phi - \Phi_c^* \Phi_c \end{array} \right] (j\omega) \geq \mathbf{0} \quad \forall \omega \in \Omega \quad (25b)$$

$$\frac{1}{2\pi} \int_{\Omega} \text{trace}(\Gamma_p(j\omega)) d\omega \leq J_p \quad (25c)$$

where $\Phi = Y_p - G_{22}X_p$ and Γ_p a Hermitian matrix function of p . Furthermore, Φ_c is chosen as $\Phi_c = Y_c - G_{22}X_c$ where $K_c = X_c Y_c^{-1}$ is a stabilizing controller to ensure closed-loop stability of the proposed scheme.

Remark 2. Under the frozen FRF assumption, the proof of stability is similar as shown in Schuchert et al. (2024), and therefore omitted. It should be noted that stability for all fixed p implies stability for sufficient slow varying $p = p(t)$ (Mohammadpour & Scherer, 2012).

In general, it is very challenging to quantify what “sufficiently slow varying” entails, but a good rule of thumb is that disturbances should be rejected much faster than the rate at which $p(t)$ changes.

A parametrization of X_p and Y_p is required to solve (25). In particular, if $X_p(j\omega)$ and $Y_p(j\omega)$ are affine in some optimization variables, then (25) is convex and corresponds to a convex semi-definite program (SDP). It is decided to take for each of the transfer functions X_p, Y_p a state-space representation of order 18. The order is chosen with the heuristic that each diagonal element of $P_p(j\omega)$ has three peaks, and the controller should be able to cancel each of these peaks, requiring three pole pairs each. For designing an LPV state-space controller of order 18, the following parametrization can be chosen:

$$X_p = \left[\begin{array}{c|c} A & B \\ \hline C_{11} + \sigma C_{12} & D_1 \end{array} \right] \quad (26a)$$

$$Y_p = \left[\begin{array}{c|c} A & B \\ \hline C_{21} + \sigma C_{22} & D_2 \end{array} \right] \quad (26b)$$

where $\sigma \in \mathbb{R}$ is the scheduling parameter, given by

$$\sigma(p) = r \quad (27)$$

The scheduling parameter is chosen as (27) since it was noted that the frequencies of the peaks in the FRF correlate well with the extension of the robotic arm, corresponding to the r position. Additional dependency on high-order terms or other components of p can be chosen, but was not required for this application. The optimization variables are $C_{11}, C_{12} \in \mathbb{R}^{3 \times 18}$, $C_{21}, C_{22} \in \mathbb{R}^{3 \times 18}$, $D_1, D_2 \in \mathbb{R}^{3 \times 3}$ which leads to affine parametrization of X_p and Y_p . $A \in \mathbb{R}^{18 \times 18}$ and $B \in \mathbb{R}^{18 \times 3}$ are fixed and can be freely chosen, provided that A is stable, the pair (A, B) is controllable, with B having full column rank. In this case, B is chosen as a matrix full of ones, and

$$A = \begin{bmatrix} \alpha_1 & 2\alpha_1 & 0 & 0 & \dots \\ 0 & \alpha_2 & 2\alpha_2 & 0 & \dots \\ \vdots & \ddots & \ddots & \ddots & \ddots \\ 0 & \dots & \dots & \dots & \alpha_N \end{bmatrix} \quad (28)$$

where α_i uniformly distributed in $[0.1, 0.9]$ and correspond to the eigenvalues of A .

A minimal realization of $K_p = X_p Y_p^{-1}$ can be obtained as shown in Schuchert et al. (2024). This reveals that 26 is a full parametrization, allowing for tuning both poles and zeros of the LPV controller:

$$K = \left[\begin{array}{c|c} A - BD_2^{-1}(C_{21} + \sigma C_{22}) & BD_2^{-1} \\ \hline (C_{11} + \sigma C_{12}) - D_1 D_2^{-1}(C_{21} + \sigma C_{22}) & D_1 D_2^{-1} \end{array} \right] \quad (29)$$

To ensure non-singularity of D_2 , it is always possible to impose $D_2 = I$.

With the parametrization proposed in 26, the optimization problem (25) becomes convex in the controller parameters, enabling the combination of multiple objectives and constraints. To enforce $\|T_{zw}\|_{\infty} \leq 1$, the following constraint can be implemented:

$$\begin{bmatrix} I & (G_{11}\Phi + G_{12}X_p) \\ \star & \Phi^* \Phi_c + \Phi_c^* \Phi - \Phi_c^* \Phi_c \end{bmatrix} (j\omega) \geq 0, \forall \omega \in \Omega \quad (30)$$

The optimization problem (18) can therefore be implemented using a combination of (25) with G_d as the augmented system, (30) with G_v as the augmented system, and the equality constraints on Y_p .

5.2. Feedforward filter

For a reference tracking problem, significantly improved performance can be obtained by adding a second path for the reference, decoupled from the feedback loop. Therefore, after the feedback controller is obtained, a feedforward filter F_p is designed.

The exact reference is not known in advance, but it is known to be similar to a ramp signal. It is therefore desired to minimize the average two-norm of the tracking error

$$\min_{F_p} \bar{J}'_p \quad (31a)$$

$$\|W_F T_{eyd}\|_2^2 \leq J'_p \quad \forall p \in \mathbb{P} \quad (31b)$$

where \bar{J}'_p is the average value of J'_p over the different operating points $p \in \mathbb{P}$. The tracking-error transfer function is given by

$$\begin{aligned} T_{eyd} &= I - (I + P_p K_p)^{-1} P_p (K_p + F) \\ &= T_{yd} (I - P_p F_p) \end{aligned} \quad (32)$$

and the weighing filter is given by

$$W_F = \frac{1}{(z-1)^2} I \quad (33)$$

Finally, an additional requirement is added to not overamplify high-frequency contents from the reference signal. This is formulated as a \mathcal{H}_{∞} norm constraint:

$$\|W_3 T_{yyd}\|_{\infty}^2 \leq 1 \quad \forall p \in \mathbb{P} \quad (34)$$

where $W_3 = 1/10$ and the transfer-function from reference y_d to the measurements y is given by

$$\begin{aligned} T_{yyd} &= (I + P_p K_p)^{-1} P_p (K_p + F) \\ &= T_{yd} P_p (K_p + F_p) \end{aligned} \quad (35)$$

The desired synthesis problem for the feedforward filter is therefore

$$\min_{F_p} \bar{J}'_p \quad (36a)$$

$$\|W_F T_{eyd}\|_2^2 \leq J'_p \quad \forall p \in \mathbb{P} \quad (36b)$$

$$\|W_3 T_{yyd}\|_{\infty}^2 \leq 1 \quad \forall p \in \mathbb{P} \quad (36c)$$

Similar to the feedback, an LPV parametrization is used for F_p such that

$$\begin{aligned} F_p &= N_p D_p^{-1} \text{ and} \\ N_p &= \left[\begin{array}{c|c} A' & B' \\ \hline C'_{11} + \sigma C'_{12} & D'_1 \end{array} \right] \end{aligned} \quad (37a)$$

$$D_p = \left[\begin{array}{c|c} A' & B' \\ \hline C'_{21} + \sigma C'_{22} & D'_2 \end{array} \right] \quad (37b)$$

and $\sigma(p) = r$.

The optimization problem (36) can be implemented using a combination of (25) with

$$G_e(j\omega) = \left[\begin{array}{c|c} W_3 T_{yd} P_p K_p & W_3 T_{yd} P_p \\ \hline I & 0 \end{array} \right] \quad (38)$$

where $T_{eyd} = F_l(G_e, F_p)$ and (30) with

$$G_y(j\omega) = \left[\begin{array}{c|c} W_3 T_{yd} & -W_3 T_{yd} P_p \\ \hline I & 0 \end{array} \right] \quad (39)$$

as the augmented system where $T_{yyd} = F_l(G_y, F_p)$. Note that the inner approximation proposed in Schuchert et al. (2024) corresponds in this case to $\Phi = D_p$ and $\Phi_c = D_c$ for some transfer function D_c with $D_c, D_c^{-1} \in \mathcal{RH}_{\infty}$. A possible choice is always $D_c = I$.

6. Experimental results

Before solving the optimization problem, remarks similar to those in Schuchert et al. (2024) are in order:

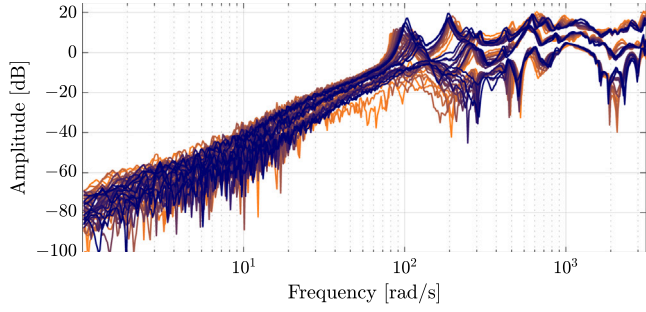


Fig. 6. Singular values of tracking error transfer function T_{ey_d} .

Remark 3. Frequency and operating points sampling: The optimization problems presented in this paper are formulated as frequency domain inequalities and correspond to solving a convex semi-infinite program (SIP). A common approach to solve such SIP is to sample the infinite number of constraints at points $\{\omega_1, \dots, \omega_{n_f}\} \in \Omega$ at a reasonably large number n_f of frequencies and operating points $p \in \mathbb{P}$. Refer to Section 4 for additional remarks about the selection of the operating points. In this case, a total of $n_f = 500$ frequencies is taken for each of the 15 models obtained from the spectral analysis, shown in Fig. 5. The different frequencies (i.e. n_f) should be chosen such that each resonant peak is sampled sufficiently densely (e.g. at least 50 frequency points for each peak), and in practice, a logarithmic grid with 400–1000 frequency points has been shown to work well on many similar problems. The integral in (25) can be approximated using a numerical integration scheme and $\Gamma_p(j\omega_k)$ can be replaced by a Hermitian auxiliary variable Γ_{pk} . Since all constraints are applied on Hermitian matrices, constraints will also be satisfied for all negative frequencies.

Remark 4. Iterative procedure: The controller obtained after solving (25) will depend on the choice of K_c , the resulting controller may be far away from a local minimum. It is proposed to solve the problem iteratively, using each time the optimal controller as the initial controller for the next iteration. The final controller will converge to a local minimum or saddle point of the original non-convex problem, see Lipp and Boyd (2016). In this case, the initial controller for the regulation loop K_{PID} is found by tuning PID controllers $K_{PID}^r, K_{PID}^\theta, K_{PID}^z$ for each of the outputs, obtained using the pidtune command in MATLAB, and then the initial controller K_c is chosen as

$$K_c = \begin{bmatrix} K_{PID}^r & 0 & 0 \\ 0 & K_{PID}^\theta & 0 \\ 0 & 0 & K_{PID}^z \end{bmatrix} \quad (40)$$

Similarly, for the feedforward, $D_c = I$ is used for the initial filter to derive the inner-approximation.

With these remarks out of the way, the (sampled frequency) optimization problem is formulated using YALMIP (Löfberg, 2004) as an intermediate modelling language and solved using the convex solver MOSEK (<https://www.mosek.com/>). Solving a single step of the iterative procedure for the feedback or feedforward requires about 90 s on a Mac Mini M2. The singular values of the various closed-loop transfer functions are shown in Figs. 6–8. In Fig. 6, the singular values of the tracking error transfer function T_{ey_d} are low when the weighting of W_o is high. Similarly, the singular values of T_{yv} and T_{yy_d} are bounded by (the inverse of) the weighting filters, as shown in Figs. 7–8. Remark that singular values of T_{yy_d}, T_{ey_d} are high for frequencies above 10^2 rad/s. This is not an issue since the reference is usually similar to a ramp and does not excite the high frequencies.

The proposed approach is implemented on the robotic arm whose FRF is shown in Fig. 5. During each single sampling period:

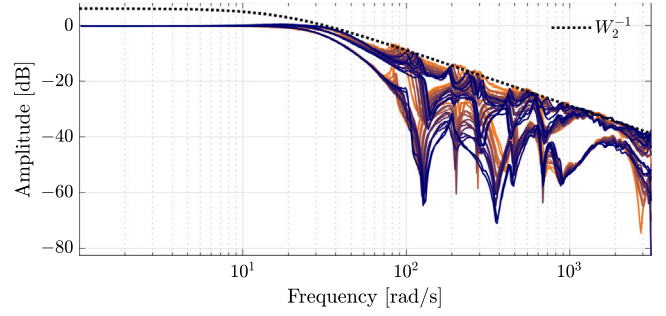


Fig. 7. Singular values of T_{yv} , along with the (inverse of) W_2 .

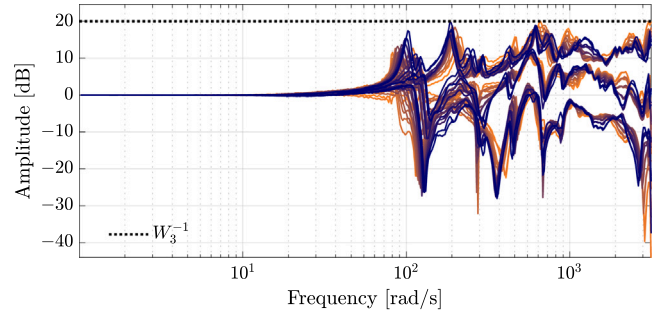


Fig. 8. Singular values of T_{yy_d} , along with the (inverse of) W_3 .

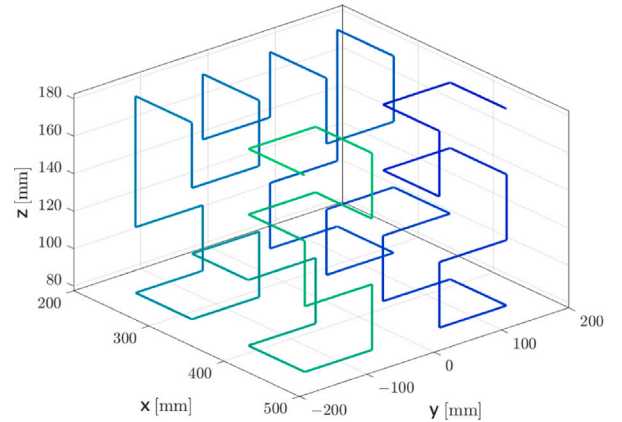


Fig. 9. Hilbert curve used for reference trajectory in tool space. Maximum speed for this reference trajectory is ≈ 100 mm/s.

- (1) At the start of the sampling period, using the measured joint positions, the forward kinematics are computed to obtain the position y in cylindrical coordinates,
- (2) The new desired input u is computed using the 2DoF controller,
- (3) The inverse kinematics are computed to obtain the desired joint positions, and the kinematic compensation is added on top.
- (4) The new reference angles for the motors are sent to the lower-level drivers at the end of the sampling period.

The robot is then tasked with tracking a reference $[x_d; y_d; z_d]$ in tool-space to benchmark performance, which comprises a Hilbert curve, shown in Fig. 9, traversing numerous operating points.

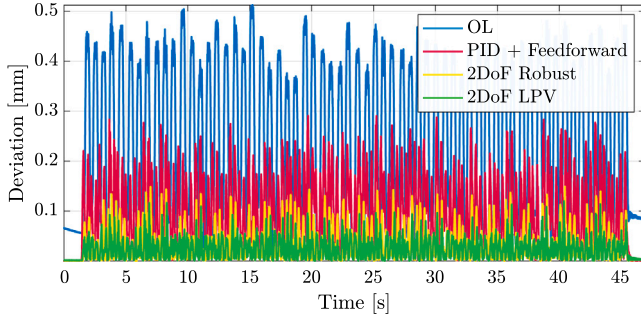


Fig. 10. Deviation reference trajectory in tool space using the different controllers.

Table 1

Performance of various control laws for the given reference trajectory. Performance corresponds to the L_2 norm of the tracking error, divided by the L_2 of the tracking error using the LPV controller.

Method	OL	PID	2DoF Robust	2DoF LPV
Perf.	8.8205	3.9110	1.3583	1

Note that this reference must first be converted into the cylindrical coordinates used in the control loop as follows:

$$y_d = \left[\text{atan2}(y_d, x_d); \sqrt{x_d^2 + y_d^2}; z_d \right].$$

Although the Hilbert curve consists only of line segments in the tool reference frame, after conversion to cylindrical coordinates, it corresponds to a curvilinear reference trajectory.

The proposed approach is compared to various approaches. First, a comparison to the open-loop, which uses only the motor driver and the inverse kinematic to compute the reference motor positions, along with the kinematic error compensation scheme. This corresponds to using $K_p = 0$, $F_p = I$. Second, a comparison with the initial PID controller K_c using as feedforward $F = I$, corresponding to the DC gain of the transfer function, is also given. Third, a comparison with a 2DoF robust controller, obtained by solving the feedback and feedforward controller using $\sigma = 0$, is also shown.

The performance is evaluated using the deviation from the reference trajectory shown in Fig. 9, and is defined as

$$\delta = \sqrt{(x - x_d)^2 + (y - y_d)^2 + (z - z_d)^2} \quad (41)$$

which corresponds to the Euclidean norm of the tracking error in tool space. The positions in tool space can be directly obtained from the cylindrical coordinates as follows:

$$[x; y; z] = [r \cos(\theta); r \sin(\theta); h] \quad (42)$$

A comparison of the deviation from the reference trajectory for both approaches is shown in Fig. 10.

A significant performance improvement can be obtained using the proposed control scheme over the open-loop, PID tracking performance, and the robust controller. Numerical values for the (normalized) performance are given in Table 1.

In particular, large tracking error peaks can be avoided when the robotic arm is accelerating due to the feedforward path. Moreover, the robot rapidly moves from one point to another without running into stability issues or significant local loss of performance, thus validating Assumption 2.

7. Conclusion

This paper proposes a data-driven method to tune LPV 2DoF controllers for robotic arms used in motion control applications. It involves obtaining frequency responses at different positions to compute a high-performance controller and compensating for transmission inaccuracies. Applied to an industrial robotic arm, it shows promising results, especially with an imposed motor loop.

CRediT authorship contribution statement

Philippe Schuchert: Writing – review & editing, Writing – original draft, Validation, Software, Methodology, Investigation, Conceptualization. **Alireza Karimi:** Writing – review & editing, Supervision, Funding acquisition.

Declaration of competing interest

The authors declare that they have no known competing financial interests or personal relationships that could have appeared to influence the work reported in this paper.

References

- Ahanda, Joseph Jean-Baptiste Mvogo, Aba, Charles Medzo, Melingui, Achile, Zobo, Bernard Essimbi, & Merzouki, Rochdi (2022). Task-space control for industrial robot manipulators with unknown inner loop control architecture. *Journal of the Franklin Institute*, 359(12), 6286–6310.
- Bagherieh, Omid, Shah, Prateek, & Horowitz, Roberto (2018). Application of mixed $\mathcal{H}_2/\mathcal{H}_\infty$ data driven control design to dual stage hard disk drives. In *Dynamic systems and control conference*, vol. 51913. American Society of Mechanical Engineers.
- Bloemers, Tom, Tóth, Roland, & Oomen, Tom (2019). Towards data-driven LPV controller synthesis based on frequency response functions. In *Proceedings of the IEEE conference on decision and control*, 2019-December (pp. 5680–5685). Institute of Electrical and Electronics Engineers Inc..
- Boerlage, Matthijs, Steinbuch, Maarten, Lambrechts, Paul, & van de Wal, Marc (2003). Model-based feedforward for motion systems. In *Proceedings of 2003 IEEE conference on control applications*, 2003. CCA 2003, vol. 2 (pp. 1158–1163). IEEE.
- Chen, Yilong (1987). Frequency response of discrete-time robot systems limitations of PD controllers and improvements by lag-lead compensation. In *Proceedings. 1987 IEEE international conference on robotics and automation*, vol. 4 (pp. 464–472). IEEE.
- De Luca, Alessandro, Siciliano, Bruno, & Zollo, Loredana (2005). PD control with on-line gravity compensation for robots with elastic joints: Theory and experiments. *Automatica*, 41(10), 1809–1819.
- Gevers, Michel (2005). Identification for control: From the early achievements to the revival of experiment design. *European Journal of Control*, 11(4–5), 335–352.
- Ghorbel, Fathi H., Gandhi, Prasanna S., & Alpetter, Friedhelm (2001). On the kinematic error in harmonic drive gears. *Journal of Mechanical Design*, 123(1), 90–97.
- Hoffmann, Christian, & Werner, Herbert (2015). A survey of linear parameter-varying control applications validated by experiments or high-fidelity simulations. *IEEE Transactions on Control Systems Technology*, 23, 416–433.
- Kammer, Christoph, & Karimi, Alireza (2017). Decentralized and distributed transient control for microgrids. *IEEE Transactions on Control Systems Technology*, 27(1), 311–322.
- Lipp, Thomas, & Boyd, Stephen (2016). Variations and extension of the convex-concave procedure. *Optimization and Engineering*, 17, 263–287.
- Löfberg, Johan (2004). YALMIP: A toolbox for modeling and optimization in MATLAB. In *2004 international conference on robotics and automation* (pp. 284–289). IEEE.
- Mohammadpour, Javad, & Scherer, Carsten W. (2012). Control of linear parameter varying systems with applications. Springer Science & Business Media.
- Oomen, Tom (2018). Advanced motion control for precision mechatronics: Control, identification, and learning of complex systems. *IEEE Journal of Industry Applications*, 7, 127–140.
- Pintelon, Rik, & Schoukens, Johan (2012). *System identification: A frequency domain approach*. John Wiley & Sons.
- Rugh, Wilson J., & Shamma, Jeff S. (2000). Research on gain scheduling. *Automatica*, 36, 1401–1425.
- Schuchert, Philippe, Gupta, Vaibhav, & Karimi, Alireza (2024). Data-driven fixed-structure frequency-based \mathcal{H}_2 and \mathcal{H}_∞ controller design. *Automatica*, 160, Article 111398.
- Schuchert, Philippe, & Karimi, Alireza (2023). Frequency-domain data-driven position-dependent controller synthesis for Cartesian Robots. *IEEE Transactions on Control Systems Technology*.
- Singer, Neil C., & Seering, Warren P. (1990). Preshaping command inputs to reduce system vibration.
- Skogestad, Sigurd, & Postlethwaite, Ian (2005). *Multivariable feedback control: Analysis and design*. John Wiley & sons.
- Vaughan, Joshua, Yano, Aika, & Singhose, William (2008). Comparison of robust input shapers. *Journal of Sound and Vibration*, 315(4–5), 797–815.
- Yamamoto, Masafumi, Iwasaki, Makoto, Hirai, Hiromu, Okitsu, Yoshifumi, Sasaki, Kozo, & Yajima, Toshio (2009). Modeling and compensation for angular transmission error in harmonic drive gearings. *IEEE Transactions on Electrical and Electronic Engineering*, 4(2), 158–165.



Philippe Schuchert received his B.Sc. and M.Sc. degrees in mechanical engineering from École Polytechnique Fédérale de Lausanne (EPFL), Lausanne, Switzerland, in 2016 and 2018, respectively. From 2018 to 2020, he was a Research Assistant with the Automatic Control Laboratory. He completed his Ph.D. degree in the doctoral program for Robotics, Control, and Intelligent Systems in 2024 at the data-driven modeling and control group of the Automatic Control Laboratory at EPFL. His research interest includes data-driven \mathcal{H}_2 and \mathcal{H}_∞ control with application to high-precision mechatronic systems.



Alireza Karimi received the Ph.D. degree from the Polytechnic National Institute of Grenoble in France, in 1997. He was an Assistant Professor with the Department of Electrical Engineering, Sharif University of Technology in Tehran, Iran, from 1998 to 2000. He then joined the École Polytechnique Fédérale de Lausanne (EPFL), Switzerland, where he is currently a Professor of automatic control with the Mechanical Engineering Institute. He is also the leader of the Data-Driven Modeling and Control Group situated at the Automatic Control Laboratory. His research focuses on data-driven controller design for power grids and mechatronic systems. Prof. Karimi contributed as an Associate Editor for the European Journal of Control between 2004 and 2013. Additionally, he has been an active member of the IEEE Control Systems Society's Conference Editorial Board since 2018.